

Modeling and inverse compensation of hysteresis in vanadium dioxide using an extended generalized Prandtl–Ishlinskii model

This content has been downloaded from IOPscience. Please scroll down to see the full text.

2014 Smart Mater. Struct. 23 125017

(<http://iopscience.iop.org/0964-1726/23/12/125017>)

View [the table of contents for this issue](#), or go to the [journal homepage](#) for more

Download details:

IP Address: 35.8.11.3

This content was downloaded on 04/01/2015 at 21:53

Please note that [terms and conditions apply](#).

Modeling and inverse compensation of hysteresis in vanadium dioxide using an extended generalized Prandtl–Ishlinskii model

Jun Zhang, Emmanuelle Merced, Nelson Sepúlveda and Xiaobo Tan¹

Department of Electrical and Computer Engineering, Michigan State University, East Lansing, MI 48824, USA

E-mail: zhangj78@egr.msu.edu, mercedem@egr.msu.edu, nelsons@egr.msu.edu and xbtan@egr.msu.edu

Received 13 June 2014, revised 25 August 2014

Accepted for publication 10 September 2014

Published 30 October 2014

Abstract

Vanadium dioxide (VO_2), a promising multifunctional smart material, has shown strong promise in microactuation, memory, and optical applications. During thermally induced insulator-to-metal phase transition of VO_2 , the changes of its electrical, mechanical, and optical properties demonstrate pronounced, complex hysteresis with respect to the temperature, which presents a challenge in the utilization of this material. In this paper, an extended generalized Prandtl–Ishlinskii model is proposed to model the hysteresis in VO_2 , where a nonlinear memoryless function is introduced to improve its modeling capability. A novel inverse compensation algorithm for this hysteresis model is developed based on fixed-point iteration with which the convergence conditions of the algorithm are derived. The proposed approach is shown to be effective for modeling and compensating the asymmetric and non-monotonic hysteresis with saturation between the curvature output and the temperature input of a VO_2 -coated microactuator, as well as the asymmetric hysteresis with partial saturation between the resistance output and the temperature input of a VO_2 film.

Keywords: Prandtl–Ishlinskii model, hysteresis, vanadium dioxide, inverse compensation

(Some figures may appear in colour only in the online journal)

1. Introduction

Vanadium dioxide (VO_2), a novel smart material, undergoes a thermally induced phase transition around 68°C [1], during which induced mechanical stress, optical transmittance, and resistance demonstrate significant changes with the temperature. These characteristics make VO_2 a promising multifunctional material for sensors [2], actuators [3], and memory applications [4]. Recently, a VO_2 -coated microactuator showed full reversible actuation, large bending around 2000 m^{-1} [3], and high energy density, showing promise in micromanipulation applications. The full utilization of this material, however, is hindered by its sophisticated hysteretic

behavior. For example, the hysteresis of a VO_2 -coated microactuator between the curvature output and the temperature input is asymmetric and non-monotonic with saturation [3], the hysteresis between the resistance output and the temperature input of a VO_2 film is asymmetric with partial saturation [5]. Without an accurate hysteresis model and proper compensation schemes, practical use of VO_2 will be limited.

Hysteresis is a nonlinearity that appears in ferromagnetic materials, various smart materials, biology, and economics. Physics-based hysteresis models usually only work for a particular material, since they are often derived based on specific physical properties [6]. Phenomenological models [7–16], on the other hand, are often constructed based on data without referring to physical properties, thus are more widely

¹ Author to whom any correspondence should be addressed.

adopted. Preisach model [7, 12] and Prandtl–Ishlinskii (PI) model [11, 17, 18] are among the most popular hysteresis models, and both have proven to be effective in hysteresis modeling and control. The Preisach model is usually expressed as a summation of weighted relay elements. In [19], the authors proposed a non-monotonic Preisach model for a VO₂-coated microactuator, where a discretization level of 20 was used for the Preisach model. The realization of the model requires tracking of hysteresis states in 210 cells with different weights, and thus the calculation and storage costs are high. PI models generally have lower computing and storage cost compared with the Preisach model [20].

The classical PI model involves the superposition of play or stop operators, and it can only capture symmetric hysteresis without output saturation. When the hysteresis is asymmetric, as observed in [5], the model will yield considerable errors. Various modifications have been proposed to cope with the limitations of the classical PI model. For example, a modified PI model was reported [21] by combining play operators with deadzone operators to model asymmetric hysteresis behavior. Furthermore, a generalized PI model uses the superposition of generalized play or stop operators [22], and has better capability to model asymmetric hysteresis with output saturation in smart materials-based systems [17]. Gu *et al* used a classical PI model in combination with a nonlinear non-hysteretic function of the input to capture the asymmetric hysteresis of piezoceramic actuators [20]. Finally, Aljanaideh *et al* proposed a rate-dependent PI model involving a memoryless function and deadband operator, and demonstrated its use in modeling the asymmetric and rate-dependent hysteresis in magnetostrictive actuators [23].

Inversion of hysteresis models is an important feedforward control approach to the compensation of hysteresis effects. Inversion of a few phenomenological models has been reported [3, 7, 9, 11, 16, 18, 21]. Unlike the Preisach model, the inverse of which is typically derived based on numerical iteration [7], analytical inversion of the classical and generalized PI models can often be derived analytically [11, 18], which facilitates the real-time control implementation. The inverse of the classical (or generalized) PI model is found to be another classical (or generalized) PI model with the same number of classical (or generalized) play operators [11, 18]. Note that analytical inversion of a generalized PI model requires all the generalized play operators to have the same envelope functions, which limits its ability in modeling complex hysteresis. For the model consisting of a classical PI operator and a memoryless function, the authors proposed an iterative scheme for its inversion [20], but the convergence of the inverse algorithm was not considered.

In this paper a hysteresis model, called *extended generalized* PI model, is proposed to capture sophisticated hysteresis as observed in VO₂. The model consists of a nonlinear memoryless function and a generalized PI model, the play operators of which have the same envelope functions. The extended generalized PI model is tested in modeling asymmetric and non-monotonic hysteresis between the curvature output and the temperature input of a VO₂-coated microactuator, demonstrating 40% less modeling error than a

generalized PI model. The advantages of the proposed model are further verified in modeling the asymmetric, partially saturated hysteresis between the resistance output and the temperature input of a VO₂ film. A novel inversion algorithm is then derived based on the fixed-point iteration framework. The convergence condition of the proposed algorithm is further derived. Finally, both simulation and experimental results are provided to support the effectiveness of the inversion algorithm. A preliminary version of this work was presented at the 2014 American Control Conference [24].

The remainder of the paper is organized as follows. In section 2, the classical and generalized PI models are briefly reviewed, and the extended generalized PI model is introduced. In section 3, the inversion scheme for the extended generalized PI model is provided. In section 4, modeling comparisons are presented to show the advantages of the proposed model over the generalized PI model. The effectiveness of the inverse compensation is verified both in simulation and experiment in section 5. Finally, concluding remarks and brief discussions on future work are presented in section 6.

2. PI models

2.1. Classical PI model

The classical PI model [25] is expressed as a weighted superposition of basic play or stop operators. As illustrated in figure 1(a), the play operator is characterized by its radius r .

The output $w(t)$ of a play operator is defined as

$$w(t) = F_r[v](t) = f_r(v(t), F_r[v](t^-)), \quad (1)$$

where

$$f_r(v(t), w(t^-)) = \begin{cases} \max(v(t) - r, w(t^-)), & \text{if } v(t) > v(t^-), \\ \min(v(t) + r, w(t^-)), & \text{if } v(t) < v(t^-), \\ w(t^-), & \text{if } v(t) = v(t^-), \end{cases} \quad (2)$$

$v(t)$ is input, and $t^- = \lim_{\epsilon > 0, \epsilon \rightarrow 0} t - \epsilon$, which denotes the immediate past time.

The output is expressed as an integral form

$$c(t) = \int_0^R p(r) F_r[v](t) dr, \quad (3)$$

where $p(r)$ is the weighting function and R represents the maximum play radius. Both $p(r)$ and R are non-negative.

For practical implementation, a weighted summation of a finite number of play operators is often adopted

$$c(t) = \sum_{j=0}^N p(r_j) F_{r_j}[v](t), \quad (4)$$

where $p(r_j)$ is the weight of the j th play operator, and r_j is the corresponding play radius. The number of play operators is $N + 1$. r_0 is usually chosen to be zero.

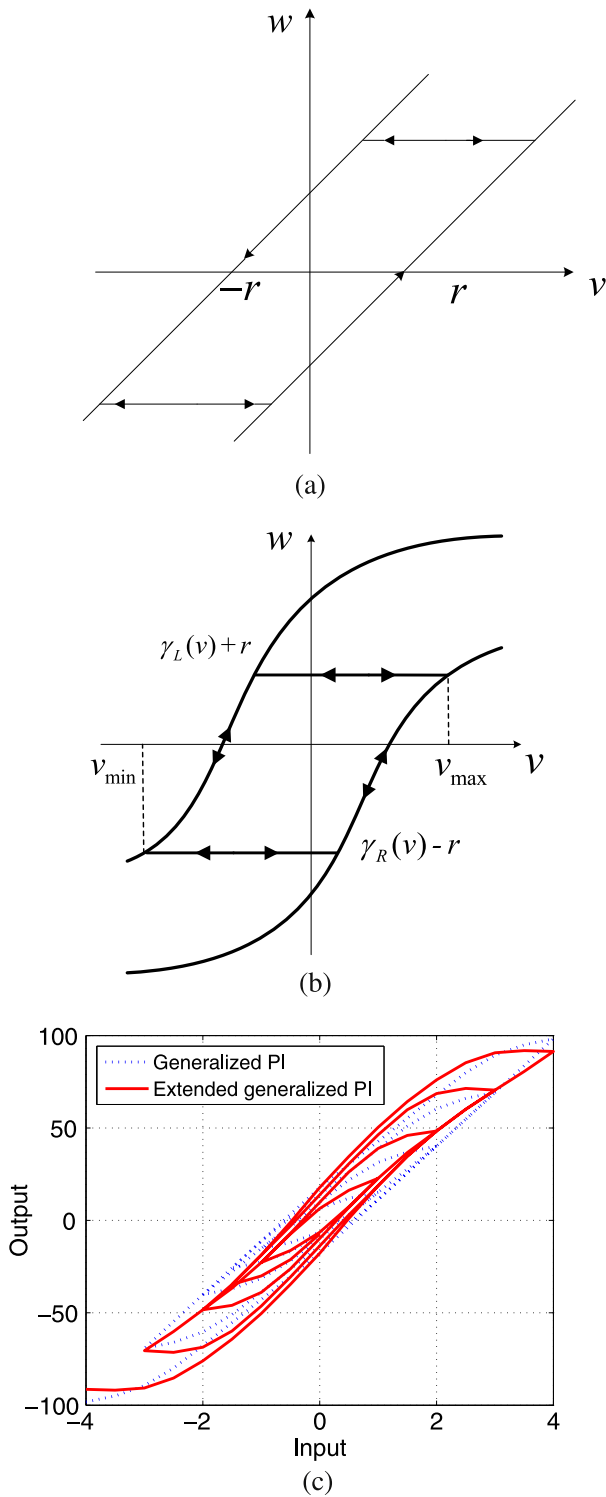


Figure 1. Input–output relationships of (a) a classical play operator; (b) a generalized play operator; (c) A generalized PI model and an extended generalized PI model with identical weights of generalized play operators.

2.2. Generalized PI model

While the classical PI model is limited to modeling symmetric and non-saturated hysteresis, the generalized PI model [17, 18] can capture more complicated hysteresis behavior.

The generalized PI model consists of a weighted superposition of generalized play operators. Following a similar treatment as in [17, 18], a generalized play operator with radius r is defined as (shown in figure 1(b))

$$w(t) = F_r^\gamma [v](t) = f_r^\gamma (v(t), F_r^\gamma [v](t^-)), \tag{5}$$

where $f_r^\gamma (t, w(t^-))$ is

$$f_r^\gamma (v(t), w(t^-)) = \begin{cases} \max (\gamma_R(v(t)) - r, w(t^-)), & \text{if } v(t) > v(t^-), \\ \min (\gamma_L(v(t)) + r, w(t^-)), & \text{if } v(t) < v(t^-), \\ w(t^-), & \text{if } v(t) = v(t^-). \end{cases} \tag{6}$$

The envelope functions for the generalized play operator, $\gamma_L(\cdot)$ and $\gamma_R(\cdot)$, are typically assumed to be strictly increasing within the input range so that they are both invertible. $\gamma_R(v(t)) - r \leq \gamma_L(v(t)) + r$ is needed to meet the order preservation property of hysteresis behavior [7].

The output of a generalized PI model is also in integral form

$$y(t) = \int_0^R p(r) F_r^\gamma [v](t) dr. \tag{7}$$

The discrete-version of the generalized PI model can be expressed as

$$y(t) = \sum_{j=0}^N p(r_j) F_{r_j}^\gamma [v](t). \tag{8}$$

The generalized PI model in equation (8) can capture asymmetric hysteresis with saturation, and it has an analytical inversion [18] as long as the envelope functions of all the generalized play operators are the same. However, the modeling capability of such a model is shown to be limited in this work.

In this paper we propose adding a nonlinear memoryless function $D(\cdot)$ to the generalized PI model:

$$u(t) = D(v(t)) + \sum_{j=0}^N p(r_j) F_{r_j}^\gamma [v](t). \tag{9}$$

This model is called the extended generalized PI model in this paper. Figure 1(c) shows a generalized PI model and an extended generalized PI model with identical weights of generalized play operators. It is shown in this paper that the extended generalized PI model can better model complex hysteresis.

3. Inversion algorithm

The goal of inverse compensation is to cancel out the hysteresis nonlinearity by constructing an inverse hysteresis model. The analytical inverse of a generalized PI model with uniform envelope functions for play operators is first reviewed. The latter will be used in the proposed fixed-point

iteration-based inversion algorithm for an extended generalized PI model.

3.1. Review of analytical inversion of generalized PI model [18]

Denote Ψ as the generalized PI model, which can be written as

$$y_d = \Psi[v](t) = \sum_{j=0}^N p(r_j) F_r^j[v](t), \quad (10)$$

where y_d is the desired output of the generalized PI model, and denote $\hat{\Psi}^{-1}$ as its approximate inverse. Then ideally,

$$y = \Psi \circ \hat{\Psi}^{-1}[y_d](t) \approx y_d, \quad (11)$$

is satisfied, where y is the actual output of the generalized PI model Ψ , and y_d is the desired output of the generalized model. Note that in inverse compensation, y_d is used as the input for the inverse model $\hat{\Psi}^{-1}$. ‘ \circ ’ denotes the composition of functions or operators. One can write

$$y(t) = \Psi[v](t), \\ = \begin{cases} \Psi[v](t) = \Pi \circ \gamma_R(v(t)), & \text{if } v(t) > v(t^-), \\ \Psi[v](t) = \Pi \circ \gamma_L(v(t)), & \text{if } v(t) < v(t^-), \\ y(t^-) & \text{if } v(t) = v(t^-), \end{cases} \quad (12)$$

where Π denotes the classical PI model.

Due to the invertibility of the envelope functions γ_L and γ_R , equation (12) can be expressed as

$$v(t) = \begin{cases} \gamma_R^{-1} \circ \Pi^{-1} \circ y(t), & \text{if } y(t) > y(t^-), \\ \gamma_L^{-1} \circ \Pi^{-1} \circ y(t), & \text{if } y(t) < y(t^-), \\ v(t^-), & \text{if } y(t) = y(t^-). \end{cases} \quad (13)$$

The inverse of the generalized PI model is written as [18]

$$\Psi^{-1}[y_d](t) = \begin{cases} \gamma_R^{-1} \circ \Pi^{-1}[y_d](t), & \text{if } y_d(t) > y_d(t^-), \\ \gamma_L^{-1} \circ \Pi^{-1}[y_d](t), & \text{if } y_d(t) < y_d(t^-), \\ \Psi^{-1}[y_d](t^-) & \text{if } y_d(t) = y_d(t^-), \end{cases} \quad (14)$$

where Π^{-1} is the inversion of the classical PI model, the expression of which can be found in [11]. The inverse of the classical PI model Π with form of equation (4) is another classical PI operator with different parameters

$$\Pi^{-1}[y](t) = \hat{p}(r_0)y(t) + \sum_{i=1}^N \hat{p}(\hat{r}_i)F_{\hat{r}_i}[y](t), \quad (15)$$

where

$$\hat{r}_j = p(r_0)r_j + \sum_{i=1}^{j-1} p(r_i)(r_j - r_i), j \geq 1, \quad (16)$$

$$\hat{p}(r_0) = \frac{1}{p(r_0)}, \quad (17)$$

and

$$\hat{p}(\hat{r}_i) = -\frac{p(r_i)}{\left(p(r_0) + \sum_{j=1}^i p(r_j)\right)\left(p(r_0) + \sum_{j=1}^{i-1} p(r_j)\right)}, \quad (18)$$

for $i = 1, \dots, N$.

3.2. Inversion of extended generalized PI model

Denote u_d as the desired output of the extended generalized PI model. Then the extended generalized PI model is expressed as

$$u_d = D(v) + \Psi[v]. \quad (19)$$

where $D(v)$ is the memoryless component and $\Psi[v]$ is the hysteresis component. Since the inversion of $\Psi[v]$ is available, rewrite equation (19) as

$$v = \Psi^{-1}[u_d - D(v)]. \quad (20)$$

Unlike the inversion of generalized PI model, $u_d - D(v)$ is used as the input for the inverse extended generalized PI model. The right part of the above equation can be solved with a known input v ; however, v is also the desired solution. To solve the problem, we first recall some background materials.

Contraction mapping [26]: Let (X, \mathbf{d}) be a metric space. A map $T: X \rightarrow X$ is called a contraction mapping on X , if there exists $q \in [0, 1)$ such that $\mathbf{d}(T(\mathbf{x}), T(\mathbf{y})) \leq q\mathbf{d}(\mathbf{x}, \mathbf{y})$ for all $\mathbf{x}, \mathbf{y} \in X$.

Proposition 1. [26]:

Let (X, \mathbf{d}) be a non-empty complete metric space with a contraction mapping $T: X \rightarrow X$. Then T admits a unique fixed point x^ in X (i.e. $T(x^*) = x^*$). Furthermore, x^* can be found as follows: start with an arbitrary element x_0 in X and define a sequence x_n by $x_n = T(x_{n-1})$, then $x_n \rightarrow x^*$.*

From proposition 1, if $\Psi^{-1}[u_d - D(v)]$ is a contraction mapping in terms of v , the inversion can be obtained by iterating $v_k = \Psi^{-1}[u_d - D(v_{k-1})]$, $k = 1, 2, \dots, n, \dots$ until $|v_n - v_{n-1}| < \sigma$, $\sigma > 0$. The following proposition provides a sufficient condition for the convergence of the inversion algorithm.

Proposition 2. *Denote $\Psi^{-1}[u_d]$ as the inversion of the generalized PI model, where u_d is the desired output. Then the operator $\Psi^{-1}[u_d - D(v)]$ is a contraction mapping on $[v_{\min}, v_{\max}]$, if*

$$\min_v \left\{ \frac{d\gamma_R}{dv}, \frac{d\gamma_L}{dv} \right\} \cdot p(r_0) > \frac{dD}{dv}. \quad (21)$$

Proof. When $u_1 > u_2$:

$$\left| \Psi^{-1}[u_1] - \Psi^{-1}[u_2] \right| \\ = \left| \gamma_R^{-1} \circ \Pi^{-1}[u_1] - \gamma_R^{-1} \circ \Pi^{-1}[u_2] \right|,$$

$$\begin{aligned}
&\leq \max_u \left\{ \frac{d\gamma_R^{-1}}{du} \right\} \cdot \left| \Pi^{-1}[u_1] - \Pi^{-1}[u_2] \right|, \\
&\leq \max_u \left\{ \frac{d\gamma_R^{-1}}{du} \right\} \cdot \hat{p}(r_0) \cdot |u_1 - u_2|, \\
&= \max_u \left\{ \frac{d\gamma_R^{-1}}{du} \right\} \cdot |u_1 - u_2|/p(r_0). \tag{22}
\end{aligned}$$

The second inequality of equation (22) holds, since

$$\begin{aligned}
&\left| \Pi^{-1}[u_1] - \Pi^{-1}[u_2] \right| \\
&= \Pi^{-1}[u_1] - \Pi^{-1}[u_2], \\
&= \hat{p}(r_0) \cdot (u_1 - u_2) + \sum_{i=1}^N \hat{p}(r_i) (F_{\hat{r}_i}[u_1](t) - F_{\hat{r}_i}[u_2](t)), \\
&\leq \hat{p}(r_0)(u_1 - u_2), \\
&= \hat{p}(r_0) \cdot |u_1 - u_2|. \tag{23}
\end{aligned}$$

The inequality of equation (23) holds since $\hat{p}(r_i) < 0$, for $i \geq 1$ (see equation (18)) and $\Pi^{-1}[u_1] \geq \Pi^{-1}[u_2]$. Similarly, for the case of $u_1 < u_2$:

$$\begin{aligned}
&\left| \Psi^{-1}[u_1] - \Psi^{-1}[u_2] \right| \\
&\leq \max_u \left\{ \frac{d\gamma_L^{-1}}{du} \right\} \cdot |u_1 - u_2|/p(r_0). \tag{24}
\end{aligned}$$

Combing the above two cases,

$$\begin{aligned}
&\left| \Psi^{-1}[u_d - D(v_1)] - \Psi^{-1}[u_d - D(v_2)] \right| \\
&\leq \max_u \left\{ \frac{d\gamma_R^{-1}}{du}, \frac{d\gamma_L^{-1}}{du} \right\} \cdot \frac{dD}{dv} \cdot |v_1 - v_2|/p(r_0), \\
&= \max_v \left\{ 1/\frac{d\gamma_R}{dv}, 1/\frac{d\gamma_L}{dv} \right\} \cdot \frac{dD}{dv} \cdot |v_1 - v_2|/p(r_0), \\
&= \frac{dD}{dv} \cdot |v_1 - v_2|/p(r_0)/\min_v \left\{ \frac{d\gamma_R}{dv}, \frac{d\gamma_L}{dv} \right\}. \tag{25}
\end{aligned}$$

Thus, $\Psi^{-1}[u_d - D(v)]$ is a contraction mapping when the following inequality is satisfied:

$$\min_v \left\{ \frac{d\gamma_R}{dv}, \frac{d\gamma_L}{dv} \right\} \cdot p(r_0) > \frac{dD}{dv}. \tag{26}$$

For classical PI model, since $d\gamma_R/dv = d\gamma_L/dv = 1$, so the convergence condition degenerates to

$$p(r_0) > \frac{dD}{dv}. \tag{27}$$

For either classical PI model or generalized PI model, since $dD/dv = 0$, no iteration is needed.

Note that, from proposition 2, the convergence of the proposed algorithm depends on the parameters of the hysteresis model.

4. Modeling performance

In this section, the modeling performance of the extended generalized PI model involving the curvature and temperature hysteresis relationship of a VO₂ coated cantilever, and the resistance and temperature hysteresis relationship of a VO₂ film are shown.

4.1. Curvature-temperature hysteresis of a VO₂-coated microcantilever

A VO₂-coated silicon micro-cantilever is subject to two actuation effects when its temperature is varied [3]. First, the stress due to thermally induced phase transition of VO₂ makes the beam bend towards the VO₂ layer, a process that is inherently hysteretic. Second, the differential thermal expansion effect generates stress in the opposite direction. As a result, the hysteresis between the bending curvature and the temperature is non-monotonic [3].

Following similar treatment [3], a 172 nm thick VO₂ layer was deposited on a silicon cantilever with length of 300 μm. The microcantilever was glued to a glass substrate that was directly in contact with a Peltier heater. A position sensitive detector (PSD) and a laser were used to measure the deflection of the microcantilever. The curvature was then obtained based on the PSD measurement.

In order to capture the hysteresis, the envelope functions for the extended generalized play operator are chosen to be hyperbolic-tangent functions in the form of

$$\gamma_R(v(t)) = \tanh(a_R v(t) + b_R), \tag{28}$$

$$\gamma_L(v(t)) = \tanh(a_L v(t) + b_L). \tag{29}$$

The non-hysteretic component is expressed as

$$D(v(t)) = p_0 \sin(\omega \cdot v(t)) + c. \tag{30}$$

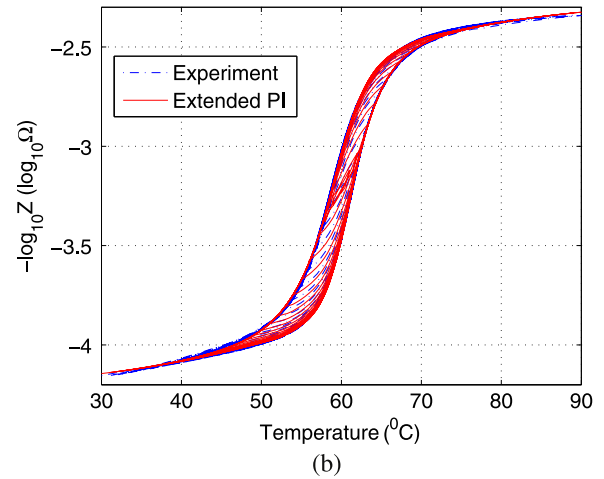
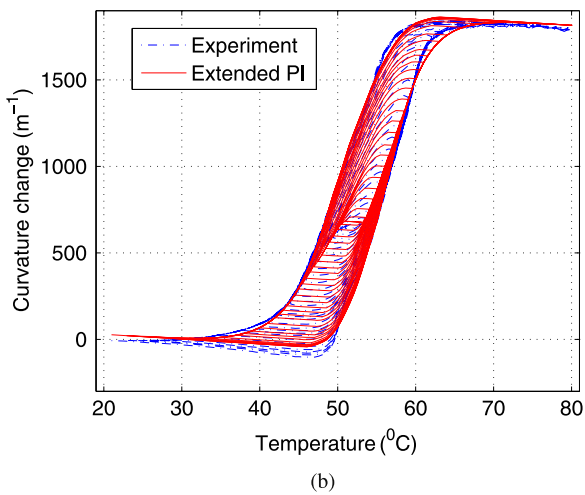
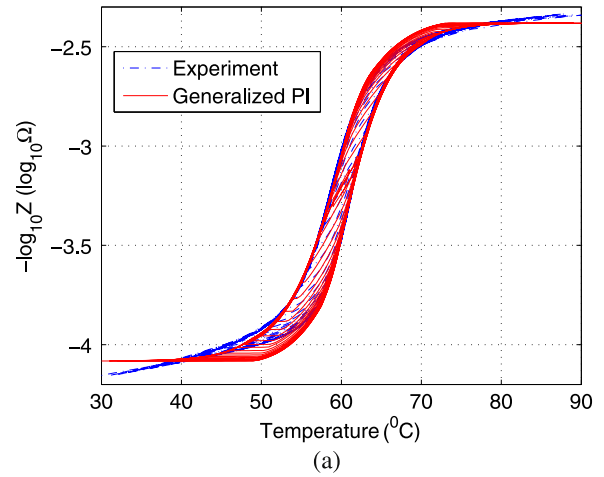
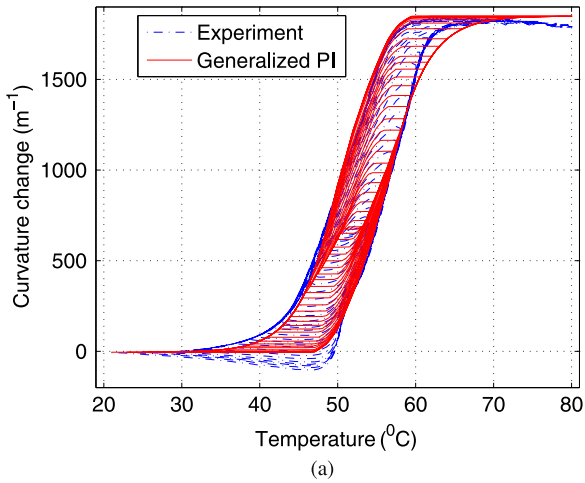
The number of the generalized play operators is chosen to be $N = 15$, and the play radii are chosen as $r = i/N$, $i = 0, 1, \dots, N - 1$. The parameters identified for the generalized PI model and the extended generalized PI model are shown in table 1. The weights of the generalized PI model and the extended generalized PI model are different due to the effect of the nonlinear memoryless function. The identified weights $p(r_i)$, $i = 0, 1, \dots, N - 1$ of both models are not included in the paper in the interest of brevity.

Note that given the envelope functions form, the identified extended PI model may not optimally model the hysteresis. The non-hysteretic component is identified as follows: first a generalized PI model is adopted to model the hysteresis, then the non-hysteretic component is chosen based on the remaining modeling error of the generalized PI model. The generalized PI model is modeled by the summation of weighted generalized play operators and an offset c .

In order to cover the whole phase transition range, the temperature range was chosen to be from 20 °C to 80 °C. In particular, we varied the temperature in repeated heating-cooling cycles with the temperature range decreased for each cycle. Figures 2(a) and (b) show the modeling performance of

Table 1. Parameters of the generalized PI model and the extended generalized PI model for hysteresis of a VO₂-coated microactuator.

	a_L	b_L	a_R	b_R	p_0	ω	c
Generalized	0.11	-5.19	0.13	-6.94	0	0	914.20
Extended	0.18	-9.61	0.14	-7.19	40.1	0.17	923.91

**Figure 2.** The performance of modeling curvature-temperature hysteresis of a VO₂-coated microcantilever based on: (a) generalized PI model. (b) Extended generalized PI model.**Figure 3.** The performance of modeling the resistance-temperature hysteresis of a VO₂ film based on: (a) generalized PI model. (b) Extended generalized PI model.

generalized PI model and that of the extended generalized PI model, respectively. Compared with the generalized PI model, the proposed model can capture the asymmetric and non-monotonic hysteresis more accurately. The root-mean-square error (RMSE) and the absolute maximum of the error are selected to quantify the modeling performance. The RSME of the generalized PI model is 38.5 m⁻¹, and the RSME of the extended generalized PI model is 26.4 m⁻¹. The largest error of the generalized PI model is 148.9 m⁻¹, while that of the extended generalized PI model is 89.6 m⁻¹. Therefore, the extended generalized PI model can capture the asymmetric and non-monotonic hysteresis behavior more accurately, with 31% and 40% smaller error in terms of RSME and the largest modeling error, respectively.

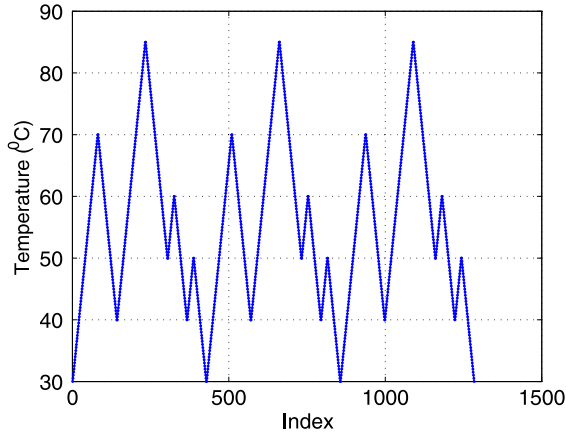
4.2. Resistance-temperature hysteresis of a VO₂ film

A VO₂ layer was deposited by pulsed laser deposition. The film was heated with a Peltier heater. The experimental setup in this work was similar to the one used in [19]. The resistance of the film was measured through two aluminium contacts patterned on the VO₂ film.

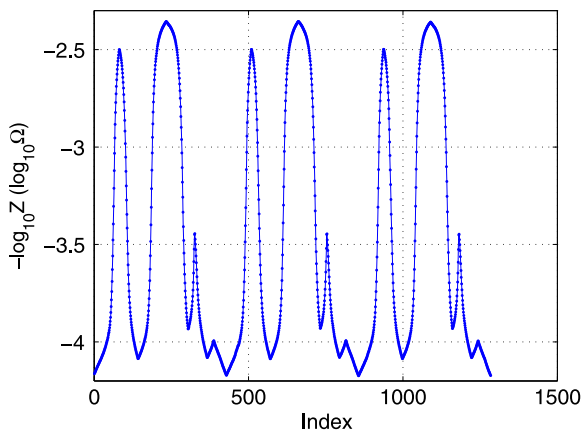
Similarly, the temperature profile in time followed a pattern of damped oscillations. It is shown in figure 3 that the measured resistance (Z) changes by approximately two orders of magnitude. Furthermore, in order to have non-negative weights for the hysteresis models, $-\log_{10}Z$ is taken as the output. The hysteresis behavior shown in figure 3 is asymmetric and also partially saturated.

Table 2. Parameters of the generalized PI model and the extended generalized PI model for hysteresis of a VO₂ film.

	a_L	b_L	a_R	b_R	p_0	a_D	b_D	c
Generalized	0.14	-8.5	0.16	-9.5	0	0	0	-3.23
Extended	0.16	-10.3	0.20	-11.6	0.4	0.03	-1.6	-3.26



(a)



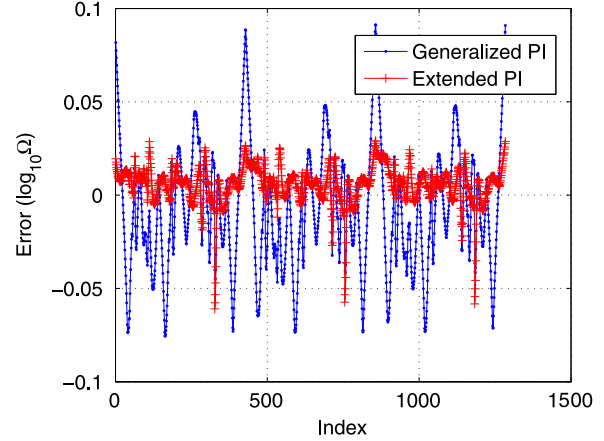
(b)

Figure 4. Model verification of the resistance–temperature hysteresis in a VO₂ film: (a) a random temperature sequence. (b) Corresponding resistance output.

Following [17, 18], the envelope functions are selected to be hyperbolic-tangent functions. The memoryless function is selected as the sum of a hyperbolic-tangent function and an offset based on the approach provided in section 5.1:

$$D(v(t)) = p_0 \cdot \tanh(a_D v(t) + b_D) + c. \quad (31)$$

The number of play operator is chosen to be $N = 30$, and the radii are chosen to be $r = i/N$, $i = 1, \dots, N$. The generalized PI model is modeled by the summation of the same number of weighted generalized play operators and an offset c . The identified parameters of the generalized PI model and the extended generalized PI model are shown in table 2. The weights of the generalized PI model and the extended generalized PI model are different due to the effect of the

**Figure 5.** Modeling comparison between the generalized PI model and extended generalized PI model.

nonlinear memoryless function. The identified weights of both models are not included due to space limitation.

Figures 3(a) and (b) show the modeling performance based on the generalized PI model and the proposed model, respectively. The RSME and the maximum absolute error of the generalized PI model are 0.031 and $0.082 \log_{10} \Omega$, respectively, while the corresponding values for the extended generalized PI model are 0.012 and $0.041 \log_{10} \Omega$, respectively. The generalized PI model has 158% and 100% larger RSME error and maximum absolute error, respectively.

Figures 4(a) and (b) show a random temperature sequence and its corresponding resistance output. The model estimation errors based on the generalized PI model and the extended generalized PI model, respectively, are shown in figure 5. The RSME and the average absolute error of the generalized PI model are 0.034 and $0.027 \log_{10} \Omega$, respectively, while the corresponding values for the extended generalized PI model are 0.012 and $0.009 \log_{10} \Omega$ respectively. The effectiveness of the extended generalized PI model in capturing the asymmetric and partial saturated hysteresis is thus further demonstrated.

5. Inverse compensation performance

Examples are shown to illustrate the effectiveness of the inverse algorithm both in simulation and experiments.

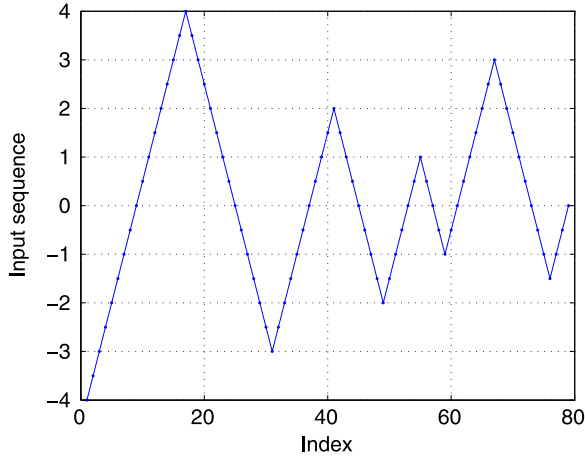
5.1. Simulation

Consider an extended generalized PI operator expressed as a memoryless function and a classical PI model, i.e.,

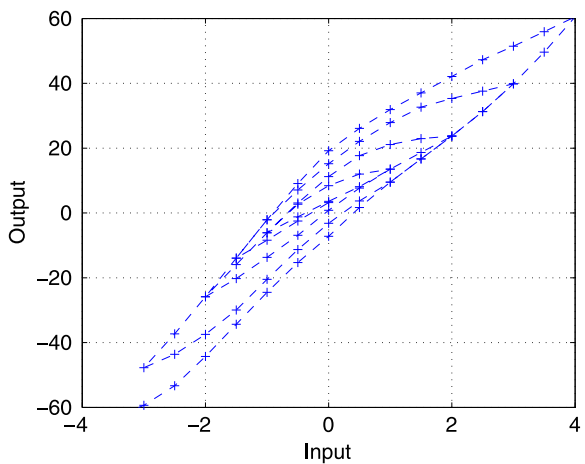
$$\gamma_R(v(t)) = v(t), \quad (32)$$

Table 3. Parameter of the extended generalized PI model.

i	1	2	3	4	5	6
r_i	0	0.2	0.4	0.6	0.8	2
$p(r_i)$	6	2	1	2	4	4



(a)



(b)

Figure 6. Simulation verification of the inverse algorithm. Hysteresis relationship: (a) input sequence. (b) Input–output of the extended generalized PI model.

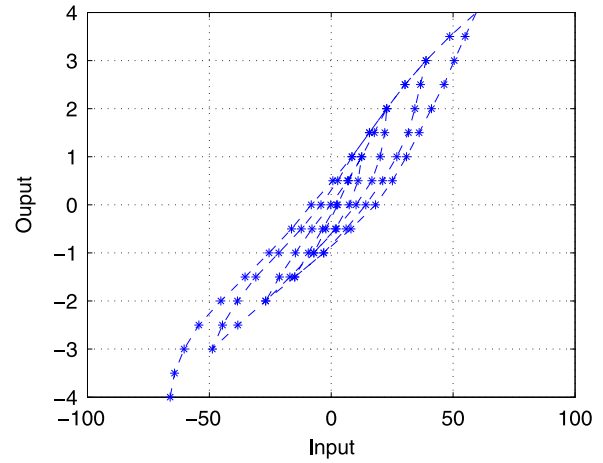
$$\gamma_L(v(t)) = v(t). \tag{33}$$

The memoryless component is chosen as

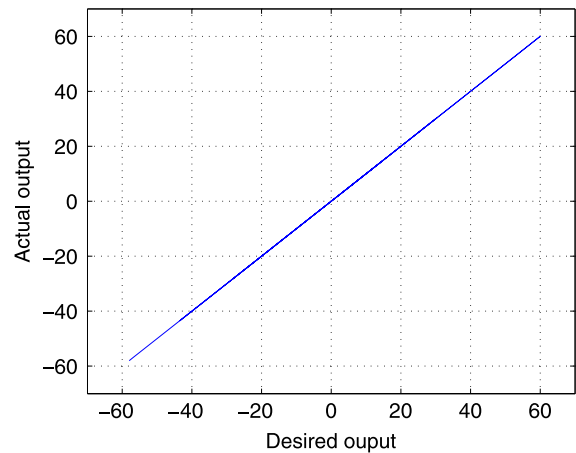
$$D(v(t)) = p_0 \cos(v(t)). \tag{34}$$

Note the envelope function and memoryless component are chosen in the above form as an illustrative example. The radii and their corresponding weights of the play operators are shown in table 3. $D(v(t))$ is chosen to be $5 \cos(v(t))$. The convergence condition for the given model is satisfied since

$$\min \left\{ \frac{d\gamma_R}{dv}, \frac{d\gamma_L}{dv} \right\} \cdot p(r_0) = 6 > 5 \geq \frac{dD}{dv}. \tag{35}$$



(a)



(b)

Figure 7. Compensation of hysteresis in simulation: (a) input–output of the inverse extended generalized PI model. (b) The relationship of the desired output and the actual output after hysteresis compensation.

Figure 6(a) shows a randomly chosen input sequence, and figure 6(b) shows the input and model output relationship. Figure 7(a) shows the inversion of the model based on the proposed algorithm, and figure 7(b) shows the resulting relationship between desired output and calculated output. The good linearity demonstrates the effectiveness of the inverse algorithm.

The average number of iterations is 8.38 when the convergence criterion σ is chosen to be 0.0001, which shows the efficiency of the algorithm. It is found in simulation that if σ is enlarged to be 0.01, the average number of iteration decreases to 5.31. It is also verified that when the value of p_0 is reduced, the inversion algorithm may not converge; on the other hand, if $p(r_0)$ remains sufficiently large, the extended generalized PI algorithm will always converge.

5.2. Experimental verification

The proposed inversion algorithm is also tested in experiments to compensate the resistance–temperature hysteresis in the

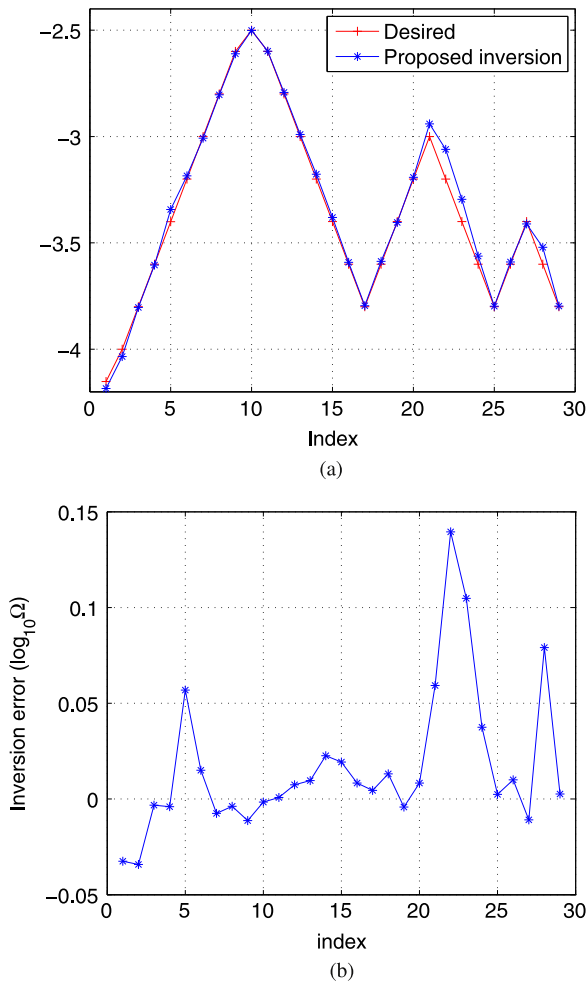


Figure 8. (a) Inverse compensation performance in experiment. (b) Inversion compensation error for the extended generalized PI model.

VO₂ film. It is verified that when the number of generalized play operators is more than 5, the modeling performance will not improve significantly while incurring higher computational cost. Therefore, a simpler and more efficient model with five generalized play operators and a nonlinear term is utilized. The parameters can be found in table 2 and [5].

It is found that when $v \in [43.2, 74.2]^\circ\text{C}$, the convergence requirement will be satisfied. Note that this covers the typical operating range for VO₂. Outside the region $[43.2, 74.2]^\circ\text{C}$, the convergence requirement may fail, since when $v \rightarrow \infty$, $dy/dv \rightarrow 0$ faster than dD/dv , and $dy/dv \ll dD/dv$, thus making equation (26) difficult to meet.

Figure 8 shows the inverse compensation performance and the inversion error. The absolute maximum inversion error is around $0.135 \log_{10}\Omega$, which still demonstrates the effectiveness of the proposed compensation approach.

6. Conclusion and future work

It was shown in this work that including a memoryless function, the modeling capability of the generalized PI model is enhanced. An inversion approach utilizing fixed-point

theory was proposed for the extended generalized PI model, along with the convergence condition. The modeling advantages of the proposed model were shown for hysteresis of a VO₂-coated microactuator and a VO₂ film, and the inversion algorithm was shown to be efficient in both simulation and experiments involving a VO₂ film.

For future work, feedback control of VO₂-coated microactuators incorporating the proposed hysteresis compensation scheme will be conducted. The inversion of the proposed model where envelope functions are different for different play operators will also be explored.

Acknowledgments

This work was supported by the National Science Foundation (CMMI 1301243). Emmanuelle Merced was supported by the National Science Foundation under Grant No. DGE-0802267 (Graduate Research Fellowships Program).

References

- [1] Marezio M, McWhan D B, Remeika J P and Dernier P D 1972 Structural aspects of the metal-insulator transitions in Cr-doped VO₂ *Phys. Rev. B* **5** 2541–51
- [2] Prasad A, Amirthapandian S, Dhara S, Dash S, Murali N and Tyagi A 2014 Novel single phase vanadium dioxide nanostructured films for methane sensing near room temperature *Sensors Actuators* **191** 252–6
- [3] Zhang J, Merced E, Sepúlveda N and Tan X 2014 Modeling and inverse compensation of non-monotonic hysteresis in VO₂-coated microactuators *IEEE/ASME Trans. Mechatronics* **19** 579–88
- [4] Cabrera R, Merced E, Dávila N, Fernández F E and Sepúlveda N 2011 A multiple-state micro-mechanical programmable memory *Microelectron. Eng.* **88** 3231–4
- [5] Zhang J, Merced E, Sepúlveda N and Tan X 2013 Optimal compression of a generalized Prandtl–Ishlinskii operator in hysteresis modeling *Proc. ASME Dynamic Systems and Control Conf.* Paper DSCC2013-3969
- [6] Harrison R 2003 A physical model of spin ferromagnetism *IEEE Trans. Magn.* **39** 950–60
- [7] Iyer R and Tan X 2009 Control of hysteretic systems through inverse compensation *IEEE Control Syst. Mag.* **29** 83–99
- [8] Lagoudas D, Hartl D, Chemisky Y, Machado L and Popov P 2012 Constitutive model for the numerical analysis of phase transformation in polycrystalline shape memory alloys *Int. J. Plast.* **32–33** 155–83
- [9] Tan X and Baras J 2004 Modeling and control of hysteresis in magnetostrictive actuators *Automatica* **40** 1469–80
- [10] Nguyen P B and Choi S B 2013 Accurate torque control of a bi-directional magneto-rheological actuator considering hysteresis and friction effects *Smart Mater. Struct.* **22** 055002
- [11] Krejci P and Kuhnen K 2001 Inverse control of systems with hysteresis and creep *IEE Proc. Contr. Theor. Ap.* **148** 185–92
- [12] Vunder V, Itik M, Poldsalu I, Punning A and Aabloo A 2014 Inversion-based control of ionic polymermetal composite actuators with nanoporous carbon-based electrodes *Smart Mater. Struct.* **23** 025010
- [13] Oh J and Bernstein D 2005 Semilinear duhem model for rate-independent and rate-dependent hysteresis *IEEE Trans. Autom. Control* **50** 631–45

- [14] Liu Y, Shan J, Gabbert U and Qi N 2013 Hysteresis and creep modeling and compensation for a piezoelectric actuator using a fractional-order maxwell resistive capacitor approach *Smart Mater. Struct.* **22** 115020
- [15] Minh T V, Tjahjowidodo T, Ramon H and Brussel H V 2011 A new approach to modeling hysteresis in a pneumatic artificial muscle using the maxwell-slip model *IEEE/ASME Trans. Mechatronics* **16** 177–86
- [16] Ikhouane F and Rodellar J 2006 A linear controller for hysteretic systems *IEEE Trans. Autom. Control* **51** 340–4
- [17] Al Janaideh M, Rakheja S and Su C Y 2009 A generalized Prandtl–Ishlinskii model for characterizing the hysteresis and saturation nonlinearities of smart actuators *Smart Mater. Struct.* **18** 045001
- [18] Al Janaideh M, Subhash R and Su C Y 2011 An analytical generalized Prandtl–Ishlinskii model inversion for hysteresis compensation in micropositioning control *IEEE/ASME Trans. Mechatronics* **16** 734–44
- [19] Zhang J, Merced E, Sepúlveda N and Tan X 2013 Kullback–Leibler divergence-based optimal compression of preisach operator in hysteresis modeling *Proc. American Control Conf. (ACC)* pp 89–94
- [20] Gu G Y, Zhu L M and Su C Y 2014 Modeling and compensation of asymmetric hysteresis nonlinearity for piezoceramic actuators with a modified Prandtl–Ishlinskii model *IEEE Trans. Ind. Electron.* **61** 1583–95
- [21] Kuhnen K 2003 Modeling, identification and compensation of complex hysteretic nonlinearities: a modified Prandtl–Ishlinskii approach *Eur. J. Control* **9** 407–18
- [22] Visintin A 1994 *Differential Models of Hysteresis (Applied Mathematical Sciences)* (Berlin: Springer)
- [23] Aljanaideh O, Rakheja S and Su C Y 2014 Experimental characterization and modeling of rate-dependent asymmetric hysteresis of magnetostrictive actuators *Smart Mater. Struct.* **23** 035002
- [24] Zhang J, Merced E, Sepúlveda N and Tan X 2014 Inversion of an extended generalized Prandtl–Ishlinskii hysteresis model: theory and experimental results *Proc. American Control Conf. (ACC)* pp 4765–70
- [25] Brokate M and Sprekels J 1996 *Hysteresis and Phase Transitions* (Berlin: Springer)
- [26] Istratescu V 2002 *Fixed Point Theory: An Introduction (Mathematics and Its Applications Series)* (London: Springer) Chapter 7